Carbohydrate Polymer Technologies and Applications 5 (2023) 100311

Contents lists available at ScienceDirect

Carbohydrate Polymer Technologies and Applications

journal homepage: www.sciencedirect.com/journal/carbohydrate-polymer-technologies-and-applications

The effects of aspect ratio of cellulose nanocrystals on the properties of all CNC films: Tunicate and wood CNCs

Amin Babaei-Ghazvini, Bishnu Acharya *

Department of Chemical and Biological Engineering, University of Saskatchewan, 57 Campus Drive, Saskatoon, SK, S7N 5A9, Canada

ARTICLE INFO

Keywords:
Cellulose nanocrystals
Tunicate CNCs
Wood CNCs
Aspect ratio
Chiral Nematic

ABSTRACT

In this study, the physicochemical, mechanical, and thermal properties of films made from cellulose nanocrystals (CNCs) obtained from two sources – wood and tunicate - and their hybrids were investigated. It was found that different morphologies affect the properties of CNC films. Specifically, the surface morphology of tunicate CNC (TCNC) films differed significantly from wood CNC (WCNC) films, and the structure of hybrid CNC (HCNC) films was also different. Compared to wood CNC-containing films, tunicate CNC films exhibited significantly higher BET surface areas, superior thermal properties, greater surface roughness, and very low (≈1 wt.%) dispersibility in water due to their ability to form long-range connectivity. The average BET surface area of TCNC films was measured at 91.9 ± 2.1 m^2/g, and this value decreased with the addition of WCNCs to the film structure. The pore diameter also decreased from 11.362 nm for TCNC films to 0.437 nm for WCNC films, indicating the filler effect of WCNCs on the TCNC films. The chiral nematic phase exhibited by WCNC films was confirmed by their iridescent appearance, as observed through cross-sectional SEM images. The TS for TCNC and HCNC3 was measured at 185.2 ± 10.5 MPa and 182.9 ± 13.7 MPa, respectively, which were the highest values among the samples. The lowest TS value of 113.1 ± 9.5 MPa was observed in the WCNC films. A similar decline was observed in the EB values, from 1.76 ± 0.37% for TCNC to 0.9 ± 0.22% for WCNC. This study provides information and knowledge useful for understanding the impact of biomass source on the properties of CNC films for a variety of purposes, including packaging materials, biodegradable coatings, flexible electronics, and membrane applications.

1. Introduction

Materials play a crucial role in nearly every product and field of technology. It is becoming increasingly important to use more sustainable materials in our daily lives due to environmental issues, climate change, and declining resources (Tang, Yang & Vignolini, 2022). Bio-based materials, such as cellulose, have significant potential to replace less eco-friendly materials in the near future. Cellulosic materials are a promising substitute for conventional polymers because of their renewability, biodegradability, exceptional mechanical and optical properties (Babaei-Ghazvini, Acharya & Korber, 2022; Chen et al., 2020; Peng et al., 2020).

A cellulose molecule is comprised of repeating units of glucose residues connected by β−1,4 glycosidic bonds, with the number of units and degrees of polymerization varying based on the source and extraction method (Habibi, Lucia & Rojas, 2010). For example, in the case of wood cellulose, these values can range from 300 to 3300, whereas for raw cotton, they fall within the range of 10,000–15,000 (Wüstenberg, 2014). Cellulose is a polymer that consists of crystalline and amorphous segments, the proportions of which are dependent on the source of the cellulose. Cellulose nanocrystals (CNCs), which are nano-sized crystalline sections, can be extracted through acid hydrolysis. A CNC macromolecule is a rod-shaped crystal with a diameter ranging from ten to twenty nanometers and a length ranging from a few hundred nanometers to several microns (Babaei-Ghazvini et al., 2020; Gao, Shang, Li & Du, 2022; Peng, Dhar, Liu & Tam, 2011). Furthermore, CNCs can also be extracted from bacteria (Iguchi, Yamanaka & Budhiono, 2000) and tunicates (Dunlop, Acharya & Bissessur, 2018). Longer CNC crystals, especially tunicate CNCs with lengths up to several microns (Dunlop et al., 2018; Moon, Martini, Nairn, Simonsen & Youngblood, 2011), can be produced from these sources.

Tunicates, as the only animals capable of producing cellulose, are well-known for the substantial amount of cellulose they generate. The unique tissue covering the epidermis of tunicates, known as the “tunic,”

* Corresponding author.
E-mail address: bishnu.acharya@usask.ca (B. Acharya).

https://doi.org/10.1016/j.carpta.2023.100311
Accepted 23 March 2023
Available online 30 March 2023

is used to store cellulose and provide skeletal support for the animal (George & Sabapathi, 2015; Trache, Hussin, Haafiz & Thakur, 2017; Wu et al., 2022; Zhao & Li, 2014). The crystalline structure of cellulose nanocrystals (CNCs) obtained from tunicates (TCNCs) is distinct from those obtained from other sources such as plant or bacterial cellulose. Tunicate cellulose is mainly composed of Iβ crystals, while CNCs obtained from wood (WCNCs) consist of both cellulose Iα and Iβ crystal structures. The ratio of Iα to Iβ in cellulose from different plants varies, with higher-order plants such as trees and shrubs containing more cellulose Iβ, while lower-order plants such as fungi and algae having more cellulose Iα (de Souza Lima & Borsali, 2004). In terms of size and aspect ratio, compared to plant sources such as wood or cotton (aspect ratio: 10–20), TCNCs have a high length-to-width ratio (70–100) and an excellent strength modulus (143 GPa) (Babaei-Ghazvini & Acharya, 2022b; Natarajan et al., 2018; Zhang et al., 2015).

Several properties of nanoparticles play an essential role in determining the mechanical, thermal, physicochemical, and photonic properties of fabricated nanocomposites. These properties include geometry, size, surface charge, surface chemistry, crystallinity, and aspect ratio (Babaei-Ghazvini & Acharya, 2022a, 2022b; Babaei-Ghazvini et al., 2020; Dunlop, Sabo, Bissessur & Acharya, 2021; Li, Wu, Moon, Hubbe & Bortner, 2021). In nature, rod-like nanomaterials such as CNCs are produced with various properties, and studying hybrid CNCs may assist in this less-studied area of science. Over the past few years, multiple types of nanoparticles have been considered for use in the production of nanocomposite materials (Babaei-Ghazvini et al., 2020; Dunlop, Acharya & Bissessur, 2020; El Miri et al., 2016; Sapkota et al., 2017; Yang et al., 2011). Further investigation is still required in the field of nanocomposite science, specifically in the area of hybrid polymeric nanocomposite materials. Due to their unique characteristics, the hybrid use of nano-scaled materials in polymeric composites can exhibit new physicochemical and mechanical properties. Several studies have shown that polymeric nanocomposites with a hybrid nano-size configuration of fillers with different morphologies exhibit better mechanical properties than mono-filler nanocomposites with the same volume fraction of fillers (El Miri et al., 2016; Sapkota et al., 2017; Yang et al., 2011). According to these studies, nano-fillers with different morphologies interact with each other to enhance mechanical performance. This paper aims to discuss the use of hybrid CNC material as an extremely elastic rod-shaped bio-based nanomaterial for physical and mechanical reinforcement. Research in this area has indicated significant potential and unique advantages in simultaneously using long and short rod-like nanomaterials (El Miri et al., 2016; Natarajan et al., 2018; Sapkota, Gooneie, Shirole, Garcia & J., 2017; Wang et al., 2021; Yang et al., 2011). In percolation theory, the percolation threshold is a mathematical concept that describes how long-range connectivity emerges in random systems. In nanocomposite studies, long-range connectivity within the polymeric network can be achieved with high aspect ratio nanoparticles. The reinforcing properties of CNCs as fillers depend on their aspect ratio and the strength of their interaction, which determines the percolation network between CNCs. (Natarajan et al., 2018) reported that the mechanical performance of all-CNC films could be enhanced by tailoring the morphology and interactions between CNCs through the addition of TCNC to WCNC films. The results demonstrated that adding small amounts of TCNC to WCNC (~5%) significantly improved the mechanical performance of the films. Although the study focused on the mechanical properties of the produced film, it did not explore the interaction between the two types of CNCs. Recently, Dunlop et al. (2020) (Dunlop et al., 2020) based on the research by Sapkota et al. (2017) (Sapkota et al., 2017) and El Miri et al. (2016) (El Miri et al., 2015), prepared T-WCNC/PVA nanocomposite. The researchers found that tunicate-derived CNCs not only display higher reinforcement than wood CNCs but also exhibit cooperative behavior when combined with WCNCs in a 1:1 ratio. Recent findings suggest that hybridizing high- and low-aspect-ratio CNCs could result in a change in the geometry of the high-aspect-ratio CNC, referred to as more surface indentation (Babaei-Ghazvini & Acharya, 2022b).

In this study, the physicochemical and mechanical properties of all-CNC films made with TCNC (long crystals), WCNC (short crystals), and the hybrid (HCNC) configuration with three different ratios were investigated. The investigation and characterization of these films may lead to the discovery of new applications, such as their use as packaging materials, biodegradable coatings, substrates for flexible electronics, and membranes for the study of biodegradable and renewable materials across various fields.

2. Materials and methods

2.1. Material

Tunicate CNC (TCNC) (1 wt.%) was prepared by hydrolyzing club tunicates with sulfuric acid according to our previously published research (Dunlop et al., 2020). Wood CNC (WCNC) gel (10 wt.%) was prepared by the sulfuric acid hydrolysis of hardwood pulp (Forest Product Laboratory, Madison, Wisconsin, United States). To compare this product with the TCNC suspension, it was diluted to 1 wt.% before use. Note that the supplementary information document includes information regarding the morphology and size distribution of the CNCs used (Table S1 and Fig. S1). All materials were used without any additional purification.

2.2. Preparation of the films

WCNC gel was diluted from 10 to 1 wt.% in order to achieve a comparable mass content between TCNC and WCNC. A well-distributed suspension of WCNCs and TCNCs, as well as a hybrid CNC suspension (HCNC), consisting of different ratios of TCNCs and WCNCs, were prepared, as shown in the Table 1. Before using the suspensions, the suspensions were stirred for 48 h at 400 rpm at room temperature and then sonicated for 1 h A 60 g of the prepared solutions were cast into a non-stick petri dish with a diameter of 15 cm and dried for 48 h at 20 °C and RH of ≈ 20% in the lab environment. Afterward, the dried films were removed from the petri dishes and stored in aluminum foil inside a desiccator at a relative humidity (RH) of 53–55% at room temperature of 20 °C for 48 h for the next stage of the study. The humidity was maintained by using a saturated magnesium nitrate ($Mg(NO_3)_2$) solution in the desiccator reported by Rockland (Rockland, 1960). Table 1 shows the abbreviation of the prepared films along with their WCNC:TCNC ratio.

2.3. Film dispersibility in water

The dispersibility of a film in water (DW) was determined by the percentage of dry matter which is dissolved in distilled water after 24 h of immersion (Gontard, Duchez, CUQ & Guilbert, 1994). To assess CNCs dispersibility in water, film samples (20 mm × 20 mm) were dried at 105 °C to reach constant weight (m_1 (g)). The dried films were submerged in 50 mL of distilled water for 24 h at 20 °C. Later, the pieces of residual film were removed and dehydrated at 105 °C to reach a constant weight (m_2 (g)). Five replications were performed for this test. The DW of the specimens was calculated using Eq. (1).

Table 1
The abbreviations and the material components of the films.

Abbreviation	Wood CNC	Tunicate CNC
WCNC	100%	–
HCNC1	75%	25%
HCNC2	50%	50%
HCNC3	25%	75%
TCNC	–	100%

$$DW = \frac{m_1 - m_2}{m_1} \times 100 \quad (1)$$

2.4. Surface area analysis

Utilizing Brunauer-Emmett-Teller (BET) techniques, the specific surface area was determined using the NOVA touch LX2 instrument. To prepare samples for measurements, ≈200 mg of the films was cut into small pieces (1 mm × 1 mm), they were placed in a glass cell for degassing for four hours at 60 °C under a vacuum of 50 mTorr. Barrett-Joyner-Halenda (BJH) method was performed for determining pore volume and pore diameter of the prepared samples.

2.5. FTIR spectroscopy

At room temperature, FTIR spectra of the film specimens were acquired using ATR-FTIR (Spectrum 3 Tri-Range MIR/NIR/FIR Spectrometer, PerkinElmer, USA). The film specimens were placed directly on the ATR crystal. FTIR spectrums were measured in the wavenumber range of 4000–600 cm^{-1} at a resolution of 4 cm^{-1}.

2.6. Differential scanning calorimetry (DSC)

A differential scanning calorimeter (DSC) was used to assess the thermal properties. The DSC Q2000 instrument was operated with nitrogen purging at a rate of 50 mL/m in order to determine the degrading point of the samples. In an aluminum pan and lid containing samples weighing 3–5 mg, the temperature was increased from 30 °C to 400 °C at a rate of 10 °C per minute.

2.7. Microstructural characterization

The microstructure of the films was examined with a scanning electron microscope (SEM). Using a Hitachi SU8010 instrument at 5 kV, SEM was performed. A double-sided carbon tape was utilized to examine both the surface and cross-sections of the film specimens after they were broken in liquid nitrogen. The specimens were coated with gold using a sputter coater (10 nm) prior to imaging. The morphology micrographs were taken with a Hitachi HT7700 transmission electron microscope (TEM). After uniformly dispersing the diluted colloidal suspension (0.001 wt.%) in water, it was cast onto etched copper-coated grids, stained with uranyl acetate, and air-dried prior to imaging. Using Image J software, 50 different measurements were taken to determine the average length and width of the micrographs. An analysis of the surface charge of the sample was performed using a Brookhaven Zeta-potential analyzer (DLS). Surface SEM images of the samples were reconstructed in MATLAB software as a 3D profile based on the recently published work (RAD, BABAEI-GHAZVINI, JAMALI, SHAHABI-GHAHFARROKHI & MORADI, 2021) to characterize surface texture.

2.8. X-ray photoelectron spectroscopy (XPS)

The XPS analysis performed at the Saskatchewan Structural Sciences Centre (SSSC) employing an AXIS Supra system from Kratos (Manchester, UK) to collect the X-ray Photoelectron Spectroscopy (XPS) data. The system uses a 500 mm Rowland circle monochromated Al K-α (1486.6 eV) source and a combined hemispherical and spherical mirror analyzer (HSA/SMA). A spot size of hybrid slot (300 × 700) microns was used. In the survey scan spectra, binding energies of 0–1200 eV were collected in steps of 1 eV with a pass energy of 160 eV The high-resolution scan collected in 0.1 eV steps. CASA XPS was used to analyze the data (Fairley et al., 2021).

2.9. Mechanical properties

Polymers' tensile strength (TS) refers to their ability to withstand the maximum tensile stress. Young's modulus is defined as the slope of the elastic area of a stress-strain curve at the breaking point. Elongation at break (EB) is defined as the change in length at the breaking point (McHugh & Krochta, 1994). TS and EB were determined using a mechanical testing instrument (Mark-10 303, USA) in accordance with ASTM standard method (D882–02). The films were cut into rectangular strips of 100 × 10 mm each and taped at the ends to make sure the jaws were not damaging the gripped area. All of the strips were conditioned at 55% RH for at least 48 h in a desiccator using saturated magnesium nitrate solution. The films were mount with an initial grip separation of 50 mm and stretched at a crosshead speed of 5 mm/min. Five replicates were carried out for each film specimen. TS and EB were calculated by Eq. (4) and Eq. (5), respectively.

$$TS = \frac{F_{Max}}{A_{Min}} \quad (4)$$

$$EB = \frac{L_{Max}}{L_0} \quad (5)$$

Where F_{Max} is the maximum load, A_{Min} is minimum cross-section area, L_{Max} is the extension at the moment of rupture, L_0 is the initial distance between the grips. Young's modulus (E) was calculated by drawing a tangent up to a strain of 0.01 of the stress-strain curves, as shown in Eq. (6).

$$YM = \frac{Stress\ (\sigma)}{Strain(\varepsilon)} \quad (6)$$

2.10. X-ray diffraction (XRD)

The powder X-ray diffraction (XRD) measurements were performed using a Bruker AXS D8 Advance instrument in reflection mode. The instrument was equipped with a graphite monochromator, variable divergence slits, variable antiscatter slits, and a scintillation detector. Cu (Kα) radiation (λ = 1.5418 Å) was used for the measurements, which were conducted at a room temperature of 2–60 ° (2θ). However, for a better comparison the diffractograms were plotted at a range of 10–30 ° (2θ).

2.11. Statistical analysis

All results were analyzed in a completely randomized design with one-way analysis of variance (ANOVA) using Minitab software (Version 18; Minitab, LLC). The difference between mean values of the properties of the film specimens was compared using Duncan's multiple range tests at the level of significance of 0.05.

3. Results and discussion

3.1. Dispersibility in water (DW)

The dispersibility of CNC films in distilled water was investigated to study the reinforcement effect, and the DW percent of the samples is shown in Fig. 1a. Since CNCs are hydroxyl-rich carbohydrates that disperse easily in water, WCNC exhibited 100% DW after the test. HCNC1 displayed a behavior similar to that of HCNC2, possibly due to the lack of network formation between the two types of CNCs. Furthermore, it was observed that DW decreased with the addition of TCNC (above 50%). The lowest DW value was measured for TCNC at 1%, while the DW value for HCNC3 was measured at 4%, confirming that as the concentration of WCNC particles in the films increases, the films become more water-sensitive. In other words, in CNC films with higher TCNC percentages, water molecules are less likely to penetrate due to the higher percolation networks resulting from TCNC (higher aspect ratio) (Sapkota et al., 2017, 2017; Wang et al., 2021). The superior aspect ratio of TCNC over WCNC can form a long-range connectivity in

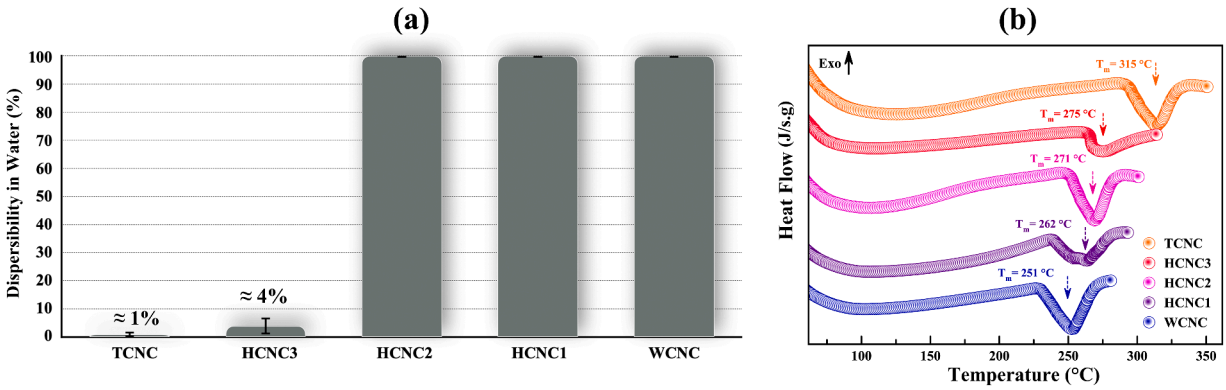

Fig. 1. (a) Dispersibility in water (DW). (b) DCS overlaid graphs of the WCNC, TCNC and HCNC with the assigned melting point temperatures from highest to lowest. In the bar chart data are means ± standard deviation as the error bar.

the all-CNC matrix, resulting in a higher level of stress being transferred from one crystal to another over a wider network of crystals. This work studied the DW of all-CNC films with the effects of CNC aspect ratio for the first time to the best of our knowledge.

3.2. *Thermal properties of the films with differential scanning calorimetry (DSC)*

On the DSC curves (Fig. 1b), an endothermic peak corresponding to the melting point temperature (T_m) of the samples was observed in the range of 200–350 °C temperature. T_m of a polymer represents the amount of energy required to disorder its crystal structure (Katritzky et al., 2001). As shown in Fig. 1b, increasing the TCNC content in the CNC films resulted in an increased T_m of the films, from WCNC (T_m =251 °C) to TCNC (T_m =315 °C). Notably, a significant 40 °C increase in T_m was observed from HCNC3 (T_m =275 °C) to TCNC (T_m =315 °C), demonstrating how the network formed by TCNC exhibits distinct thermal properties compared to the other samples. The high aspect ratio and crystallinity of TCNC particles contribute to the formation of these networks.

3.3. *Crystal structure analysis with X-ray diffraction (XRD)*

XRD diffractograms (Fig. 2a) showed the presence of cellulose I crystal structures in WCNC, TCNC, and their hybrids, with strong peaks observed at 14.7°, 16.8°, and 22.8°, corresponding to (1$\bar{1}$0), (110), and (200) crystal planes, in agreement with similar studies (Dunlop et al., 2020; Zhao, Moser, Lindström, Henriksson & Li, 2017). TCNC ideally has a parallelogram shape in cross-section, with Iβ crystal structure, but acid hydrolysis used for TCNC extraction causes partial corrosion of the parallelogram shape. Consequently, the cross-section appears as a distorted hexagon, with (1$\bar{1}$0), (110), and (200) terminating surfaces and (1$\bar{1}$0) being the largest surface (Fig. 2c) (Helbert, Nishiyama, Okano & Sugiyama, 1998; Moon et al., 2011). As shown in Fig. 2a, the X-rays diffracted from the (1$\bar{1}$0) crystal lattice for TCNC and the (200) crystal lattice for WCNC exhibit higher intensities than the other two crystal lattices, in accordance with existing literature (Zhao et al., 2017). In the hybrid samples, an increase in WCNC concentration in TCNC films led to an increase in peak intensity at (200), while the peak intensity at (1$\bar{1}$0) decreased.

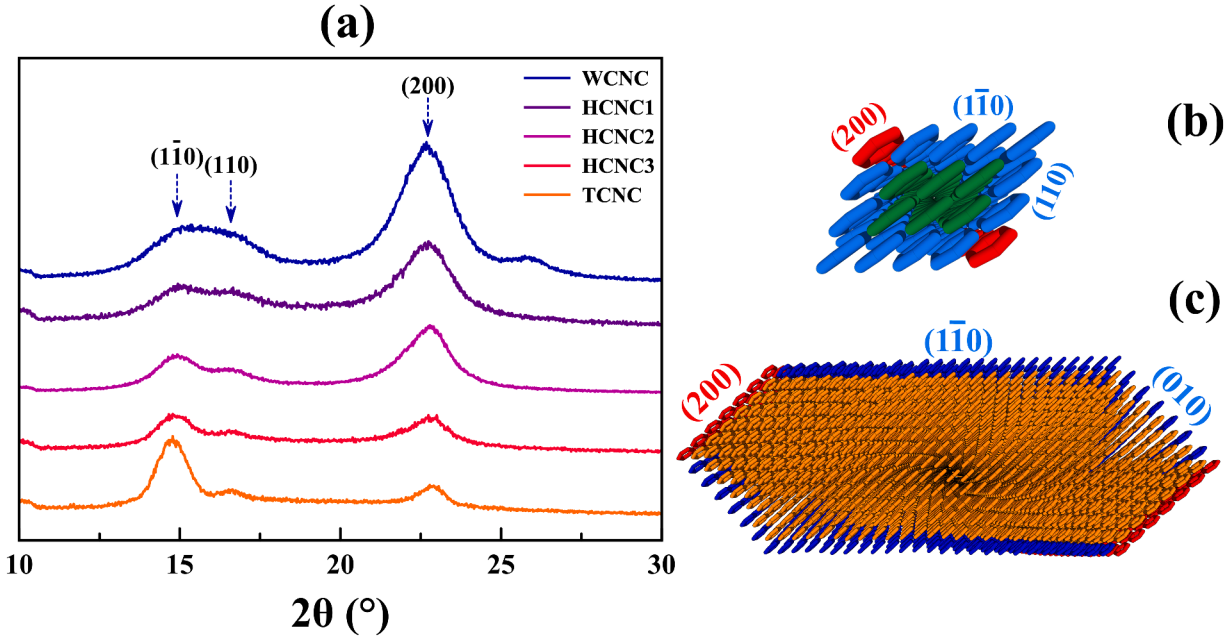

Fig. 2. (a) Stacked XRD spectra of WCNC, HCNC1, HCNC2, HCNC3, and TCNC. cross-sectional illustration of (b) WCNC crystal structure and (c) TCNC crystal structure, with the colored hydrophilic OH sides (1$\bar{1}$0), (110) in blue and the hydrophobic CH sides in red (200).

3.4. Hydrogen-bonding analysis with FTIR spectroscopy

Several studies have investigated the attribution of different bands in the cellulose band spectrum. Maréchal and Chanzy have provided a detailed description of the various bands comprising the spectrum of cellulose (Maréchal & Chanzy, 2000). Fig. 3 displays the FTIR spectrum of CNC films, with the characteristic peaks of CNCs and cellulose observed to be generally similar. A broad absorbance band has been observed for CNC films at 3200–3400 cm^{-1}, which corresponds to the stretching vibration of the OH groups in cellulose. Typically, this OH-related peak is observed in lignocellulosic biomass materials owing to the hydroxyl-rich nature of lignin, hemicelluloses, cellulose, and pectin. This spectral region is characterized by a broad band with two visible peaks at 3334 and 3276 cm^{-1}. The methylene C—H stretching band has been identified in the spectral region 3100–2700 cm^{-1}, with an arrow being placed at 2902 cm^{-1}. Five other signals have been observed and marked with an arrow in the figure at 1645 cm^{-1}, 1164 cm^{-1} and 1111 cm^{-1}, 1055 cm^{-1}, and 1033 cm^{-1} (Babaei-Ghazvini & Acharya, 2022b; Cherian et al., 2008; Zhou et al., 2018). The highly coupled OH stretch vibration modes are a result of hydrogen-bonding interactions within the cellulose crystal. As illustrated in Fig. 3, the peak at ≈3276 cm^{-1} in cellulose can be attributed to OH vibrations, with a significant contribution from intrachain H-bonds from C_2—OH groups. The peak at ≈3407 cm^{-1} is significantly influenced by interchain H-bonded C_6—OH groups, while the peak at ≈3334 cm^{-1} has a significant contribution from intrachain H-bonded C_{2-3-6}—OH groups (Lee et al., 2015). The strong peaks at 3407 cm^{-1} and 3334 cm^{-1} were observed in both TCNC and HCNC3, primarily due to the presence of interchain H-bonded C_6—OH groups. The higher crystallinity of TCNC (80–95%) compared to WCNC (45–60%), and its larger crystal size, attributed to its structure having more glucose units (and consequently, more interchain H-bonded C_6—OH), may explain this observation (Dhali, Ghasemlou, Daver, Cass & Adhikari, 2021; Dunlop et al., 2020, 2020). The 1645 cm^{-1} band (OH bending) shown as an inset in the plot indicates the presence of water molecules bonded to the hydrophilic surface of CNCs (Rosa et al., 2010; Souza et al., 2015; Yunos, Baharuddin, Yunos, Naim & Nishida, 2012). The intensity of the peaks decreased as the concentration of TCNC increased from WCNC to TCNC, confirming a reduction in the number of water molecules bonded to the CNC particles. This observation may be attributed to the larger surface area of WCNC resulting from their smaller crystal size, which enables them to retain more water.

Regarding the signals on the right side of the spectrum (1400–700 cm^{-1}), the peak at 1164 cm^{-1} is associated with the antisymmetric stretching of the C—O bridge, while the peak at 1111 cm^{-1} represents the glucose skeletal stretch of C—OH. Finally, the signals at 1055 cm^{-1} and 1033 cm^{-1} are associated with the C—O-C pyranose ring (Zhao et al., 2017). A small peak at 895 cm^{-1} corresponds to the glycosidic -CH deformation in cellulose, with a ring vibration and -OH twisting in the β-glycosidic linkages between the glucose molecules (Sun, Sun, Zhao & Sun, 2004). The peak at 710 cm^{-1} indicates the presence of the cellulose Iβ structure (Sugiyama, Persson & Chanzy, 1991), which was prominent in the TCNC and HCNC3 samples, confirming that the films have a structure more similar to tunicate CNCs. The peak area of TCNC films at 710 cm^{-1} was higher than that of HCNC3, suggesting that the surface of TCNC particles is partially covered with WCNC particles. Upon closer inspection of these samples in this spectral region, it was observed that HCNC2, HCNC1, and WCNC exhibited similar characteristics to WCNC.

3.5. Surface chemistry analysis with X-ray photoelectron spectroscopy (XPS)

Samples of WCNC, TCNC, and HCNC were analyzed using X-ray photoelectron spectroscopy to determine their surface chemistry. By analyzing the elemental composition, atomic and mass concentrations of the samples using XPS, a better understanding of their surface chemistry could be gained. Fig. 4a-b-c displays a higher resolution spectrum of WCNC, TCNC, and HCNC, along with their assigned signals representing oxygen (O1s, 530–532 eV), nitrogen (N1s, 396–400 eV), and carbon (C1s, 284–288 eV) (Abitbol, Johnstone, Quinn & Gray, 2011; Rahmani, Ashori & Varnaseri, 2016; Sadasivuni et al., 2015). Based on the high-resolution O1s spectra presented in Fig. 4a, WCNC exhibits a slight shift towards lower binding energies compared to TCNC. This shift may be attributed to the higher concentration of sulfate groups ($-SO3^-$) present on the surface of WCNC. It has been reported in surface chemistry studies of CNCs that the presence of sulfate groups can cause a shift in the O1s spectra (Friedman, Shi, Losovyj, Siedle & Baker, 2018; Hood et al., 2018; Wei, Fahlman & Epstein, 1999). The N1s spectra presented in Fig. 4b indicate a small peak at around 399 eV for TCNC, suggesting the presence of nitrogen atoms on the surface of the CNCs. This occurrence could be due to residual protein or amino acids remaining on the surface of TCNC after CNCs isolation. The absence of this peak in the

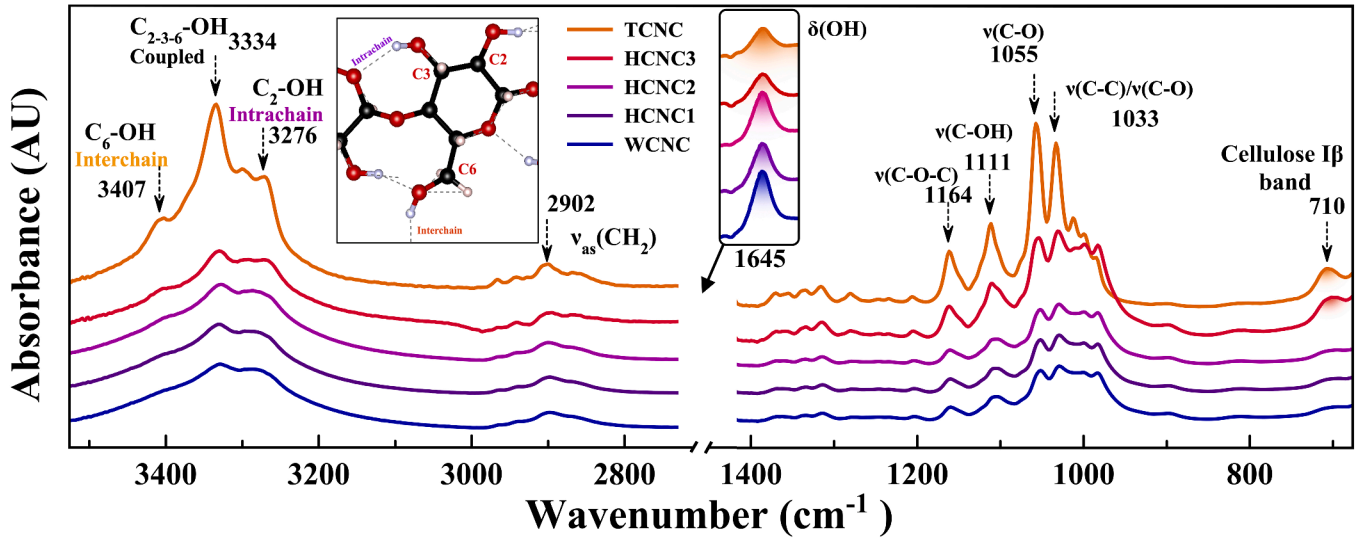

Fig. 3. FTIR absorbance overlaid graphs of the WCNC, TCNC, and the hybrid films. (Left inset) Hydroxyl groups geometry of cellulose Iβ molecule in VESTA (Momma & Izumi, 2011) software based on the cellulose Iβ crystallography study (Nishiyama, Langan & Chanzy, 2002). (Right inset) magnified 1645 cm^{-1} band. Symbols description: ν, stretch; δ, bending deformation; as, antisymmetric.

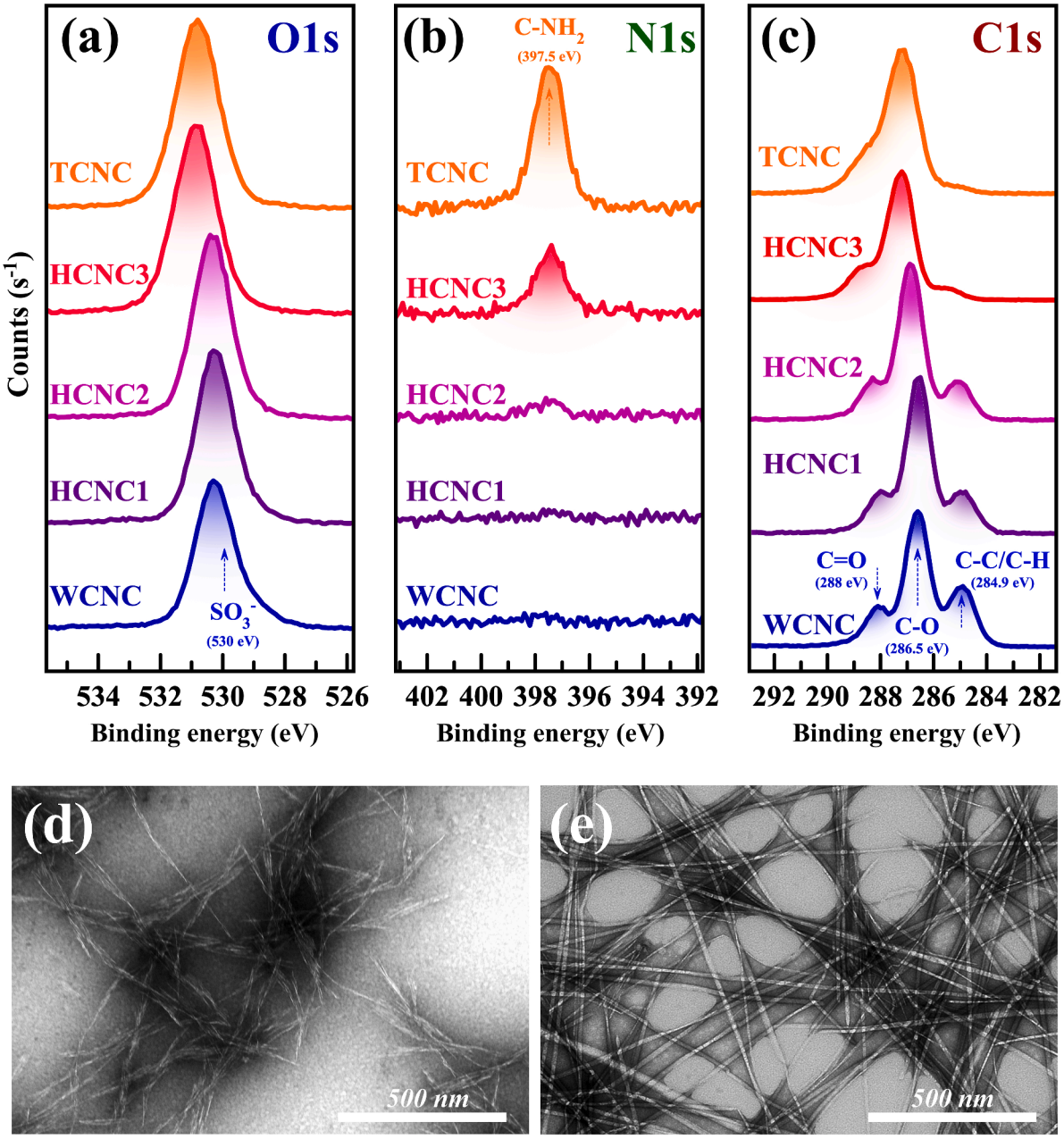

Fig. 4. High-resolution XPS spectra for WCNCs, TCNCs, and HCNCs. Signal assignments in different binding energies (a) O1s for oxygen, (b) N1s for nitrogen, (c) C1s for carbon. TEM micrographs, (d) WCNCs and (e) TCNCs.

other samples suggests that their surfaces are not significantly contaminated with protein residues. However, it should be noted that the N1s signal is weak and may be challenging to detect in samples with low levels of contamination. The high-resolution XPS spectra for WCNC and TCNC display three peaks associated with (C–C/C–H), (C–O), and (C = O) groups at 284.9, 286.5, and 288 eV, respectively. In the C1s region, a noticeable change in the peak (C–C/C–H) at the binding energy of 284.9 eV was observed. The WCNC spectrum displayed a much more intense shoulder compared to the TCNC spectrum. The decrease in the peak intensity of (C–C/C–H) with increasing TCNC content may be attributed to the dilution effect of TCNC particles in the hybrid structure. Conversely, the significant decrease in the HCNC3 sample suggests that the surface of TCNC particles is covered with WCNC particles, resulting in a decrease in the exposure of the (C–C/C–H) group to the surface. The peak associated with (C–O) groups at 286.5 eV is more prominent in the TCNC sample than in the WCNC sample, which could be attributed to the higher crystallinity of TCNC. Finally, the peak associated with (C = O) groups at 288 eV is more intense in the WCNC sample, which may be related to the higher concentration of sulfate groups on the WCNC surface. XPS was used as a surface chemistry study method, and based on recent findings regarding the surface interaction between TCNC and WCNC, it was expected that such behavior would occur when the hybrid CNCs contents were varied (Babaei-Ghazvini & Acharya, 2022b). It was anticipated that if the concentration of WCNC to TCNC exceeded ≈ 25 wt.%, the surface of TCNC would be covered by WCNC particles, and to some extent, TCNC would not be available on the surface. The findings of this study for N1s and C1s can be explained by this behavior, which will be discussed in detail in the morphological studies section.

3.6. CNCs morphology, film structure, and BET surface area analysis

The morphology of CNCs was examined using transmission electron

microscopy (TEM). The images revealed that WCNCs were generally shorter than TCNCs (Fig. 4d-e), which could be attributed to the different sources of cellulose. Tunicates are known to produce longer and more uniform cellulose nanocrystals than wood. The difference in morphology could have significant implications for potential applications, such as in the reinforcement of materials. SEM images of surface sections of CNC films are shown in Fig. 5a-b. TCNC films had larger particles on their surface, which were distinguishable from those on WCNC films. These results were consistent with the TEM images presented in Fig. 4d-e. TCNCs formed a network with more voids due to their larger particle size compared to WCNCs, which is consistent with previous literature (Zhao et al., 2017). On the surface of WCNC films, particles were aligned in the same direction, corresponding to the surface nematic layer of WCNC, indicating the formation of a chiral nematic structure (Babaei-Ghazvini & Acharya, 2021; Babaei-Ghazvini et al., 2022; Majoinen, Kontturi, Ikkala & Gray, 2012).

A significant role is played by surface geometry and morphology in determining the physical properties of coatings, including water absorption, water contact angle, and gas barrier properties. Hence, to assess their importance, the surface topography and profilometry of the produced coatings were further investigated using 3D volumetric image processing in MATLAB. The porosity and structure of CNC films also have a significant impact on their applications. The micron-scale representation of the 3D reconstructed surface topology, as shown in Fig. 5c, illustrates that a higher degree of surface roughness is observed in TCNC films. The addition of WCNCs to the TCNC matrix results in a smoother surface, and at higher concentrations of WCNC, the low aspect ratio particles fill into the pores on all sides of the TCNC particles. Consequently, WCNC primarily functions as a filler in the TCNC matrix. Fig. 5e displays the cross-section profilometry derived from the surface topographies shown in Fig. 5c using green arrowed lines (point A to B). The peaks and valleys of the surface of the TCNC films ($\approx 41 \pm 12$ nm) are more prominent in comparison to the other samples, confirming the filler effects caused by the addition of WCNC. In both HCNC2 and HCNC1, the peaks and valleys fluctuated around zero ($\approx 5 \pm 2$ nm), indicating the smooth surface of the samples.

The cross-section of the films can reveal their structural organization when analyzed with SEM. Therefore, during film formation, the chiral nematic or random alignment of the CNCs can be investigated. Fig. 5d illustrates the cross-sectional SEM images from the samples. Stacked layers of randomly aligned CNCs were observed for TCNC. A similar structure was reported in the literature (Babaei-Ghazvini & Acharya, 2022b; Huang et al., 2021). WCNC films exhibited iridescent colors (Fig. S2) and displayed a chiral nematic organization, as seen in the cross-section SEM images. The chiral nematic phase of the CNC films is responsible for reflecting structural colors under Bragg's regime, which distinguishes it from the other phases in terms of its visual properties (Kelly, Giese, Shopsowitz, Hamad & MacLachlan, 2014). Structural color was not observed for the HCNC films (Fig. S2). The study of the chiral nematic phase revealed that the self-assembly of WCNCs could be affected by the hybrid configuration, and a change in particle size distribution could interfere with this process. However, some reports have shown structural color reflections with low concentrations (up to 10 wt. %) of TCNC in WCNC, which was lower than the ratios (25 wt.%) investigated in our study (Natarajan et al., 2018). Additionally, a study on colorimetry was conducted on film samples, and the findings revealed that the addition of TCNCs to the all-CNC films resulted in an increase in the yellowness index (YI) of the films. The colorimetry table is presented in the supporting information (Table S2).

A complementary study was conducted on the surface area of the films using the BET method. The CNC films were analyzed using this method, as shown in Fig. 5-f-g. Nitrogen gas adsorption-desorption isotherms and calculated surface areas at liquid nitrogen temperatures (−196 °C) were measured and shown in the figure. The BET surface area for CNCs materials may differ due to the sample preparation and source of the CNC. Based on the literature to date, freeze-dried CNCs samples have shown a greater surface area in comparison with CNC films. According to Lu and Hsieh (Lu & Hsieh, 2010), CNCs isolated from cotton cellulose had a BET surface area of 13.36 m^2/g. Another study conducted by (Abu-Danso, Srivastava, Sillanpää & Bhatnagar, 2017) estimated the surface area of CNCs to be approximately 8 m^2/g based on their BET method. The surface area of cotton sourced CNCs was found to be 1.3 m^2/g based on the measurements obtained from BET analysis (Mohamed et al., 2022). A surface area of ≈55–59 m^2/g was reported for bacterial-sourced CNCs using a freeze-dried sample preparation method at liquid nitrogen temperature, as measured with the BET method by Kondor et al. (2021). The reported surface area value for bacterial CNCs was higher than the reported surface area value of plant-based CNCs due to its higher aspect ratio (Kondor et al., 2021). In this study, the average BET surface area of TCNC films was measured to be 91.9 ± 2.1 m^2/g using a nitrogen gas adsorption technique. This value was found to be higher than the surface area value of 31.4 m^2/g reported by Zhao et al. Different sources and extraction methods used in each work may have contributed to the difference in values (Zhao et al., 2017). The presence of sulfate-half ester groups on the surface of the CNCs, which were isolated using sulfuric acid hydrolysis, led to strong repulsion forces in suspension and the formation of light-weight and porous films. Additionally, TCNCs have the highest aspect ratio among all reported types of CNCs to date (Moon et al., 2011), allowing for the formation of long-range connectivity in their films (Sapkota et al., 2017). Upon adding 25 wt.% WCNCs to the TCNCs structure, the adsorption volume decreased considerably from 170 cc/g to 5.5 cc/g, as shown in the adsorption isotherms (Fig. 5f). This confirms that WCNCs acted as fillers in the TCNCs matrix. The isotherm plots for all samples, except TCNC, are presented in Fig. 5g, and it is evident that the volume of adsorption significantly decreased with increasing amounts of WCNC in the matrix.

The Barrett-Joyner-Halenda (BJH) desorption method was used to obtain the total pore volume and pore diameter of all samples. Table 2 presents the results obtained from the BJH desorption method. The total pore volume of TCNCs was found to be 0.2610 cm^3/g, which was significantly higher than the total pore volume of the other samples. The addition of WCNCs to the TCNC films caused a considerable reduction in pore volume, with HCNC3 having a pore volume of 0.0084 cm^3/g. The total pore volume of the other samples was found to be negligible, which was consistent with the BET adsorption-desorption isotherms. The pore diameter decreased significantly from 11.362 nm for TCNC films to 0.437 nm for WCNC films, as reported in Table 2. These results confirm that WCNCs had more of a filler effect on the films' structure, and films with higher TCNC content exhibited slightly larger pore diameter due to the higher aspect ratio of TCNCs.

3.7. Mechanical properties of the CNC films

Fig. 6a shows the stress-strain curves of the samples, and Fig. 6b presents a graph of the elastic moduli of the films on the right side of the assigned stress-strain curves. The CNC films displayed highly elastic behavior, with EBs below 2%. The TS of TCNC and HCNC3 was measured at 185.2 ± 10.5 MPa and 182.9 ± 13.7 MPa, respectively, which were the highest values among the samples. Huang et al. (2021) reported a TS of 140.3 MPa for tunicate cellulose films, which was consistent with the measured value for TCNC (Huang et al., 2021). Zhao et al. reported a TS of 177.5 ± 20.3 MPa for tunicate cellulose fiber films (Zhao et al., 2017). No significant decrease in TS was observed for HCNC3, which may be attributed to the percolating threshold achieved and maintained by TCNCs, even with the addition of WCNCs to their structure. The network formed and maintained by TCNCs facilitates stress transfer between CNC particles. As mentioned earlier, the addition of WCNCs up to 25% did not negatively impact the shear and stress transfer, thereby preserving the mechanical performance of the HCNC3 films. However, the TS of the rest of the hybrid CNC films decreased with the addition of WCNCs. For HCNC2 and HCNC1, the TS decreased to 158.8 ± 5.7 MPa and 131.5 ± 8.5 MPa, respectively, from the initial TS

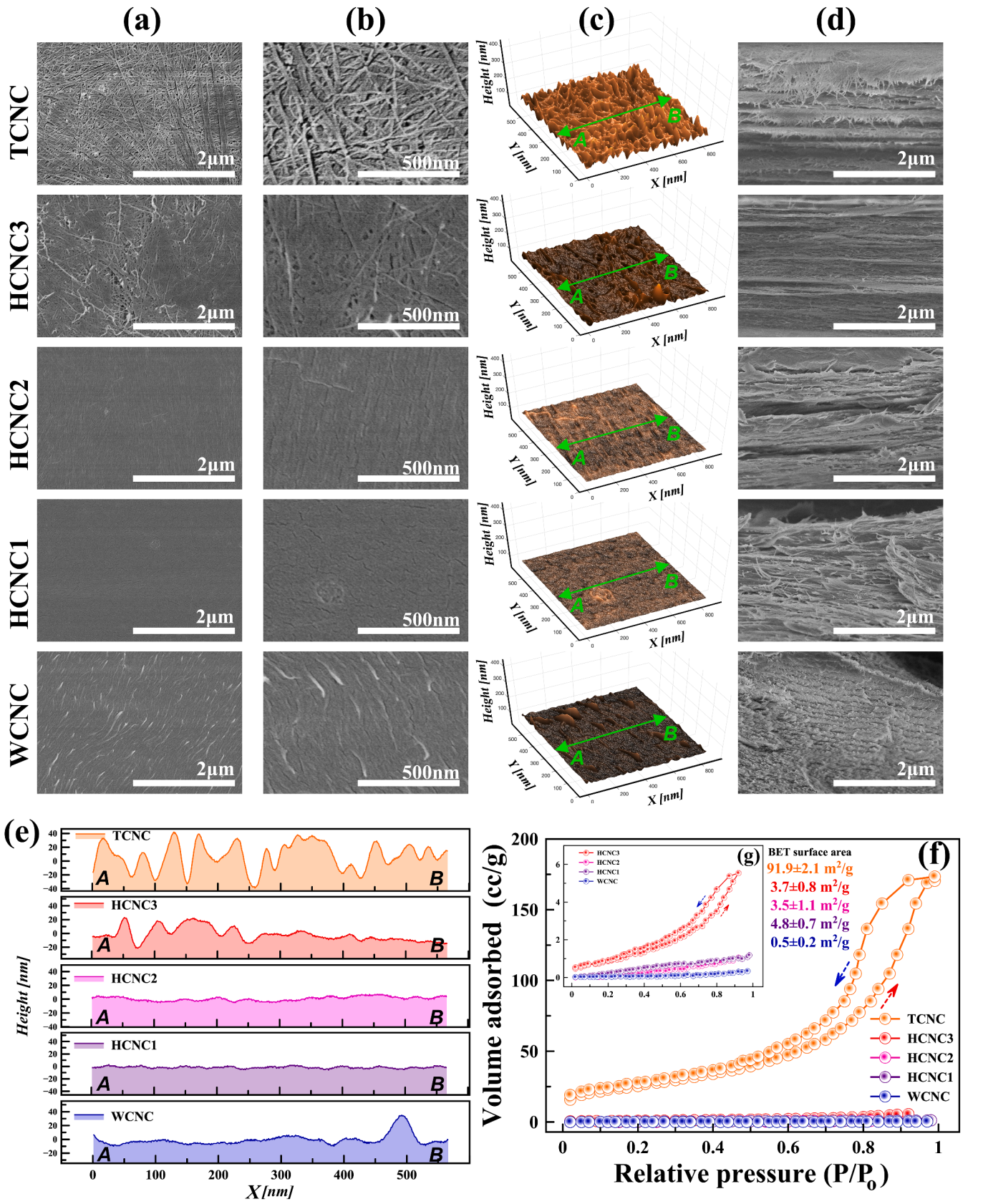

Fig. 5. (a) surface SEM images, (b) surface SEM images with higher magnification. (c) The corresponding 3D reconstructed images of the films surfaces. (d) Cross-sectional SEM micrographs of CNC films. (e) cross-section profilometry from point A to B. (f-g) adsorption-desorption isotherms of the CNC films with BET surface areas as the inset.

Table 2
Characteristics of BET and BJH analysis table [‡], [*].

Abbreviation	BET surface area (m^2/g)	Total pore volume (cm^3/g)	Pore diameter (nm)[a]
WCNC	0.5 ± 0.2^c	0.0005 ± 0.0001^c	0.437 ± 0.239^c
HCNC1	4.8 ± 0.7^b	0.0018 ± 0.0009^b	2.539 ± 0.975^c
HCNC2	3.5 ± 1.1^b	0.0016 ± 0.0011^b	8.734 ± 2.385^b
HCNC3	3.7 ± 0.8^b	0.0084 ± 0.0013^b	9.544 ± 1.973^b
TCNC	91.9 ± 2.1^a	0.2610 ± 0.0118^a	11.362 ± 3.754^a

[‡] Means within each column with the same letters are not significantly different ($P<0.05$).
[*] Data are means ± SD.
[a] Determined by BJH method.

of 182.9 MPa for HCNC3. The lowest TS value of 113.1 ± 9.5 MPa was observed in the WCNC films, which may be attributed to the lower degree of connectivity in the network formed by these particles. A similar trend to the changes in TS values was observed in the EB values when WCNC was added to TCNC, with a decrease from 1.76 ± 0.37% for TCNC to 0.9 ± 0.22% for WCNC, as shown in Fig. 6a. The decrease in TS and EB may be attributed to the smaller particle size and reduced stress transfer resulting from the low aspect ratio of the WCNC. These values were consistent with reported values for wood and tunicate cellulose films in similar studies (Huang et al., 2021; Zhao et al., 2017). The stress-strain curves in Fig. 6a were used to calculate the elastic modulus of the film specimens shown in Fig. 6b. No clear trend in the nanocomposite's elasticity was observed, but the E values for TCNC and HCNC2 were higher than those for the other films. Unfortunately, due to the lack of similar works in the literature, we were unable to compare these values with published data. To the best of our knowledge, the only reported value in the literature for tunicate cellulose fiber films was 12.6 ± 0.1 GPa, which was higher than the value we obtained. This value was reported by (Zhao et al., 2017). It is worth noting that the brittleness and rigidity of all-CNC films can make it challenging to measure their mechanical properties accurately. Therefore, the mechanical properties of all-CNC films may vary from one study to another.

4. Conclusions

The effects of wood-sourced CNCs and tunicate-sourced CNCs, along with their hybrids with varying aspect ratios, on the film-forming properties of all-CNC films was investigated in this study. The physicochemical and mechanical properties of nanocomposites were examined in order to develop sustainable and biodegradable materials. Results revealed that TCNC films exhibited 1% dispersibility in water, while the addition of WCNC to their structure increased their sensitivity to water. As the TCNC content increased in the CNC films, the T_m of the films rose from 251 °C for WCNCs to 315 °C for TCNCs. SEM images showed that WCNC films displayed iridescent colors and were in the chiral nematic phase, which disappeared after the addition of TCNCs to the film's structure. The XPS results indicated that the surface chemistry of the films became similar to that of WCNCs when the WCNCs content was 50% or higher, suggesting that the TCNCs were covered by the WCNCs on the surface. The surface area of TCNC films was measured at 91.9 ± 2.1 m^2/g, which is the highest reported value to date, and significantly decreased with the addition of WCNC. The addition of WCNCs to the CNC film structure resulted in a decrease in TS values, indicating that the mechanical strength of the film was reduced. These changes in the mechanical performance of the films may be attributed to the lower aspect ratio of WCNCs compared to TCNCs, resulting in less efficient stress transfer between particles and a less connected network. The findings of this study may benefit the development of all-CNC films as sustainable and biodegradable materials for packaging, biomedical, and membrane applications.

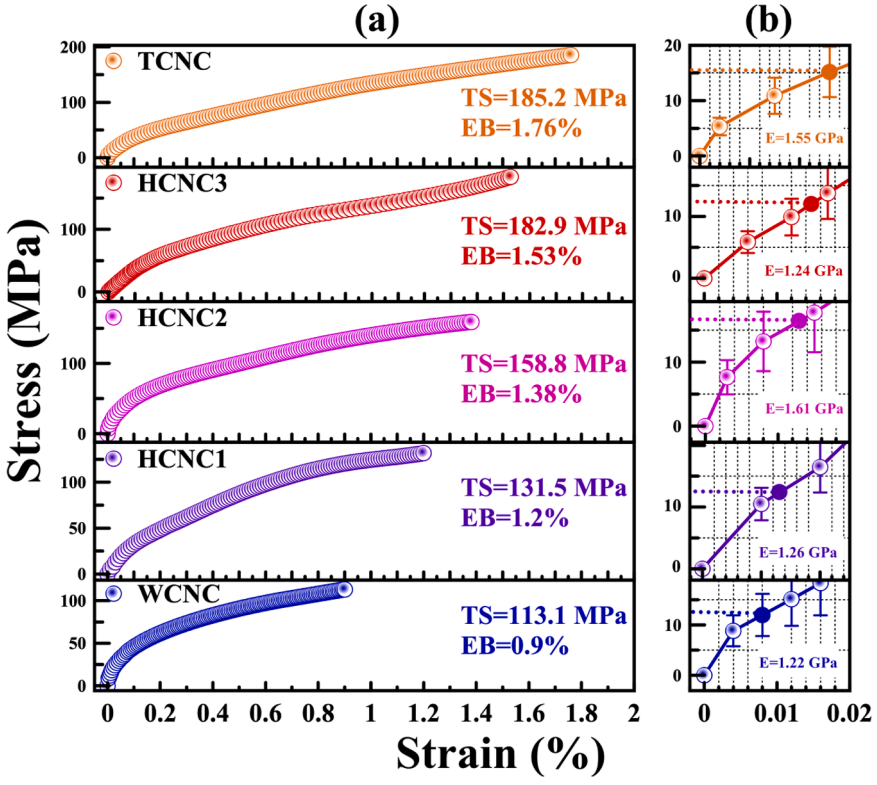

Fig. 6. Mechanical properties stress-strain curves (a) top to bottom: TCNC, HCNC3, HCNC2, HCNC1, and WCNC. Elastic modulus (E) was calculated by drawing a tangent up to a strain of 1% of the stress-strain curves, (b) top to bottom: TCNC, HCNC3, HCNC2, HCNC1, and WCNC.

Associated content

Ethics approval and consent to participate

Not applicable.

Consent for publication

Authors give permission for publication of all data, images, details, and information.

CRediT authorship contribution statement

Amin Babaei-Ghazvini: Conceptualization, Literature review, Writing - original draft, Writing - review & editing, Visualization. **Bishnu Acharya:** Conceptualization, Supervision, Funding acquisition, Writing - review & editing, Resources.

Funding sources

The work was supported by Natural Science and Engineering Research Council Discovery Grant program [RGPIN-2022-05111] and Saskatchewan Ministry of Agriculture Research Chair Funds.

Supporting Information

This information includes the morphology of the CNCs used, the surface charge, digital images from the CNC films, and colorimetry results.

Declaration of Competing Interest

The authors declare that they have no known competing financial interests or personal relationships that could have appeared to influence the work reported in this paper.

The authors declare the following financial interests/personal relationships which may be considered as potential competing interests:

Data availability

Partially available in the supplementary information.

Acknowledgments

The Saskatchewan Structural Sciences Centre (SSSC) is acknowledged for providing facilities to conduct this research. Funding from Canada Foundation for Innovation, Natural Sciences and Engineering Research Council of Canada and the University of Saskatchewan support research at the SSSC.

Supplementary materials

Supplementary material associated with this article can be found, in the online version, at doi:10.1016/j.carpta.2023.100311.

References

Abitbol, T., Johnstone, T., Quinn, T. M., & Gray, D. G. (2011). Reinforcement with cellulose nanocrystals of poly (vinyl alcohol) hydrogels prepared by cyclic freezing and thawing. *Soft matter, 7*(6), 2373–2379.

Abu-Danso, E., Srivastava, V., Sillanpää, M., & Bhatnagar, A. (2017). Pretreatment assisted synthesis and characterization of cellulose nanocrystals and cellulose nanofibers from absorbent cotton. *International Journal of Biological Macromolecules, 102*, 248–257.

Babaei-Ghazvini, A., & Acharya, B. (2021). Humidity-Responsive Photonic Films and Coatings Based on Tuned Cellulose Nanocrystals/Glycerol/Polyethylene Glycol. *Polymers, 13*(21). https://doi.org/10.3390/polym13213695

Babaei-Ghazvini, A., & Acharya, B. (2022a). Crosslinked poly (vinyl alcohol) composite reinforced with tunicate, wood, and hybrid cellulose nanocrystals: Comparative physicochemical, thermal, and mechanical properties. *International Journal of Biological Macromolecules*. https://doi.org/10.1016/j.ijbiomac.2022.11.281

Babaei-Ghazvini, A., & Acharya, B. (2022b). Influence of cellulose nanocrystal aspect ratio on shear force aligned films: Physical and mechanical properties. *Carbohydrate Polymer Technologies and Applications*, Article 100217.

Babaei-Ghazvini, A., Acharya, B., & Korber, D. R. (2022). Multilayer photonic films based on interlocked chiral-nematic cellulose nanocrystals in starch/chitosan. *Carbohydrate Polymers, 275*, Article 118709. https://doi.org/10.1016/j.carbpol.2021.118709

Babaei-Ghazvini, A., Cudmore, B., Dunlop, M. J., Acharya, B., Bissessur, R., Ahmed, M., et al. (2020). Effect of magnetic field alignment of cellulose nanocrystals in starch nanocomposites: Physicochemical and mechanical properties. *Carbohydrate Polymers*, Article 116688.

Chen, H., Hou, A., Zheng, C., Tang, J., Xie, K., & Gao, A. (2020). Light-and humidity-responsive chiral nematic photonic crystal films based on cellulose nanocrystals. *ACS Applied Materials & Interfaces*.

Cherian, B. M., Pothan, L. A., Nguyen-Chung, T., Mennig, G., Kottaisamy, M., & Thomas, S. (2008). A novel method for the synthesis of cellulose nanofibril whiskers from banana fibers and characterization. *Journal of Agricultural and Food Chemistry, 56*(14), 5617–5627.

de Souza Lima, M. M., & Borsali, R. (2004). Rodlike cellulose microcrystals: Structure, properties, and applications. *Macromolecular Rapid Communications, 25*(7), 771–787.

Dhali, K., Ghasemlou, M., Daver, F., Cass, P., & Adhikari, B. (2021). A review of nanocellulose as a new material towards environmental sustainability. *Science of The Total Environment*, Article 145871.

Dunlop, M. J., Acharya, B., & Bissessur, R. (2018). Isolation of nanocrystalline cellulose from tunicates. *Journal of Environmental Chemical Engineering, 6*(4), 4408–4412.

Dunlop, M. J., Acharya, B., & Bissessur, R. (2020). Study of plant and tunicate based nanocrystalline cellulose in hybrid polymeric nanocomposites. *Cellulose (London, England), 27*(1), 249–261. https://doi.org/10.1007/s10570-019-02791-5

Dunlop, M. J., Clemons, C., Reiner, R., Sabo, R., Agarwal, U. P., Bissessur, R., et al. (2020). Towards the scalable isolation of cellulose nanocrystals from tunicates. *Scientific Reports, 10*(1), 1–13.

Dunlop, M. J., Sabo, R., Bissessur, R., & Acharya, B. (2021). Polylactic acid cellulose nanocomposite films comprised of wood and tunicate CNCs modified with tannic acid and octadecylamine. *Polymers, 13*(21), 3661.

El Miri, N., Abdelouahdi, K., Barakat, A., Zahouily, M., Fihri, A., Solhy, A., et al. (2015). Bio-nanocomposite films reinforced with cellulose nanocrystals: Rheology of film-forming solutions, transparency, water vapor barrier and tensile properties of films. *Carbohydrate Polymers, 129*, 156–167.

El Miri, N., El Achaby, M., Fihri, A., Larzek, M., Zahouily, M., Abdelouahdi, K., et al. (2016). Synergistic effect of cellulose nanocrystals/graphene oxide nanosheets as functional hybrid nanofiller for enhancing properties of PVA nanocomposites. *Carbohydrate Polymers, 137*, 239–248.

Fairley, N., Fernandez, V., Richard-Plouet, M., Guillot-Deudon, C., Walton, J., Smith, E., et al. (2021). Systematic and collaborative approach to problem solving using X-ray photoelectron spectroscopy. *Applied Surface Science Advances, 5*, Article 100112.

Friedman, A. K., Shi, W., Losovyj, Y., Siedle, A. R., & Baker, L. A. (2018). Mapping microscale chemical heterogeneity in Nafion membranes with X-ray photoelectron spectroscopy. *Journal of The Electrochemical Society, 165*(11), H733.

Gao, M., Shang, Y., Li, B., & Du, H. (2022). Sustainable preparation of cellulose nanocrystals: State of the art and perspectives. *Green Chemistry*.

George, J., & Sabapathi, S. N. (2015). Cellulose nanocrystals: Synthesis, functional properties, and applications. *Nanotechnology, Science and Applications, 8*, 45.

Gontard, N., Duchez, C., CUQ, J., & Guilbert, S. (1994). Edible composite films of wheat gluten and lipids: Water vapour permeability and other physical properties. *International Journal of Food Science & Technology, 29*(1), 39–50.

Habibi, Y., Lucia, L. A., & Rojas, O. J. (2010). Cellulose nanocrystals: Chemistry, self-assembly, and applications. *Chemical Reviews, 110*(6), 3479–3500.

Helbert, W., Nishiyama, Y., Okano, T., & Sugiyama, J. (1998). Molecular imaging ofhalocynthia papillosacellulose. *Journal of Structural Biology, 124*(1), 42–50.

Hood, Z. D., Adhikari, S. P., Evans, S. F., Wang, H., Li, Y., Naskar, A. K., et al. (2018). Tire-derived carbon for catalytic preparation of biofuels from feedstocks containing free fatty acids. *Carbon Resources Conversion, 1*(2), 165–173.

Huang, D., Li, D., Mo, K., Xu, R., Huang, Y., Cui, Y., et al. (2021). Top-down fabrication of biodegradable multilayer tunicate cellulose films with controlled mechanical properties. *Cellulose (London, England), 28*(16), 10415–10424.

Iguchi, M., Yamanaka, S., & Budhiono, A. (2000). Bacterial cellulose—A masterpiece of nature's arts. *Journal of Materials Science, 35*(2), 261–270.

Katritzky, A. R., Jain, R., Lomaka, A., Petrukhin, R., Maran, U., & Karelson, M. (2001). Perspective on the relationship between melting points and chemical structure. *Crystal Growth & Design, 1*(4), 261–265.

Kelly, J. A., Giese, M., Shopsowitz, K. E., Hamad, W. Y., & MacLachlan, M. J. (2014). The development of chiral nematic mesoporous materials. *Accounts of Chemical Research, 47*(4), 1088–1096.

Kondor, A., Santmarti, A., Mautner, A., Williams, D., Bismarck, A., & Lee, K.-. Y. (2021). *On the BET surface area of nanocellulose determined using volumetric, gravimetric and chromatographic adsorption methods*.

Lee, C. M., Kubicki, J. D., Fan, B., Zhong, L., Jarvis, M. C., & Kim, S. H. (2015). Hydrogen-bonding network and OH stretch vibration of cellulose: Comparison of computational modeling with polarized IR and SFG spectra. *The Journal of Physical Chemistry B, 119*(49), 15138–15149.

Li, M., Wu, Q., Moon, R. J., Hubbe, M. A., & Bortner, M. J. (2021). Rheological aspects of cellulose nanomaterials: Governing factors and emerging applications. *Advanced Materials, 33*(21), Article 2006052.

Lu, P., & Hsieh, Y.-. L. (2010). Preparation and properties of cellulose nanocrystals: Rods, spheres, and network. *Carbohydrate Polymers, 82*(2), 329–336.

Majoinen, J., Kontturi, E., Ikkala, O., & Gray, D. G. (2012). SEM imaging of chiral nematic films cast from cellulose nanocrystal suspensions. *Cellulose (London, England), 19*(5), 1599–1605.

Maréchal, Y., & Chanzy, H. (2000). The hydrogen bond network in Iβ cellulose as observed by infrared spectrometry. *Journal of Molecular Structure, 523*(1–3), 183–196.

McHugh, T. H., & Krochta, J. M. (1994). Sorbitol-vs glycerol-plasticized whey protein edible films: Integrated oxygen permeability and tensile property evaluation. *Journal of Agricultural and Food Chemistry, 42*(4), 841–845.

Mohamed, S. H., Hossain, M. S., Kassim, M. H. M., Balakrishnan, V., Habila, M. A., Zulkharnain, A., et al. (2022). Biosorption of Cr (VI) Using Cellulose Nanocrystals Isolated from the Waterless Pulping of Waste Cotton Cloths with Supercritical CO2: Isothermal, Kinetics, and Thermodynamics Studies. *Polymers, 14*(5), 887.

Momma, K., & Izumi, F. (2011). VESTA 3 for three-dimensional visualization of crystal, volumetric and morphology data. *Journal of Applied Crystallography, 44*(6), 1272–1276.

Moon, R. J., Martini, A., Nairn, J., Simonsen, J., & Youngblood, J. (2011). Cellulose nanomaterials review: Structure, properties and nanocomposites. *Chemical Society Reviews, 40*(7), 3941–3994.

Natarajan, B., Krishnamurthy, A., Qin, X., Emiroglu, C. D., Forster, A., Foster, E. J., et al. (2018). Binary cellulose nanocrystal blends for bioinspired damage tolerant photonic films. *Advanced Functional Materials, 28*(26), Article 1800032.

Nishiyama, Y., Langan, P., & Chanzy, H. (2002). Crystal structure and hydrogen-bonding system in cellulose Iβ from synchrotron X-ray and neutron fiber diffraction. *Journal of the American Chemical Society, 124*(31), 9074–9082.

Peng, B. L., Dhar, N., Liu, H. L., & Tam, K. C. (2011). Chemistry and applications of nanocrystalline cellulose and its derivatives: A nanotechnology perspective. *Canadian Journal of Chemical Engineering, 89*(5), 1191–1206. https://doi.org/10.1002/cjce.20554. Wiley Online Library.

Peng, N., Huang, D., Gong, C., Wang, Y., Zhou, J., & Chang, C. (2020). Controlled arrangement of nanocellulose in polymeric matrix: From reinforcement to functionality. *ACS nano, 14*(12), 16169–16179.

Rad, V. F., Babaei-Ghazvini, A., Jamali, R., Shahabi-Ghahfarrokhi, I., & Moradi, A.-R. (2021). Digital holographic microscopy for real-time investigation of 3D microstructural dynamics of starch-kefiran based nanocomposite. *Applied Optics, 60*, 4706–4715.

Rahmani, H., Ashori, A., & Varnaseri, N. (2016). Surface modification of carbon fiber for improving the interfacial adhesion between carbon fiber and polymer matrix. *Polymers for Advanced Technologies, 27*(6), 805–811.

Rockland, L. B. (1960). Saturated salt solutions for static control of relative humidity between 5° and 40°C. *Analytical Chemistry, 32*(10), 1375–1376.

Rosa, M. F., Medeiros, E. S., Malmonge, J. A., Gregorski, K. S., Wood, D. F., Mattoso, L. H. C., et al. (2010). Cellulose nanowhiskers from coconut husk fibers: Effect of preparation conditions on their thermal and morphological behavior. *Carbohydrate Polymers, 81*(1), 83–92.

Sadasivuni, K. K., Kafy, A., Zhai, L., Ko, H., Mun, S., & Kim, J. (2015). Transparent and flexible cellulose nanocrystal/reduced graphene oxide film for proximity sensing. *Small (Weinheim an der Bergstrasse, Germany), 11*(8), 994–1002.

Sapkota, J., Gooneie, A., Shirole, A., & Garcia, J. C. M. (2017a). A refined model for the mechanical properties of polymer composites with nanorods having different length distributions. *Journal of Applied Polymer Science, 134*(36), 45279.

Sapkota, J., Shirole, A., Foster, E. J., Garcia, J. C. M., Lattuada, M., & Weder, C. (2017b). Polymer nanocomposites with nanorods having different length distributions. *Polymer, 110*, 284–291.

Souza, N. F., Pinheiro, J. A., Silva, P., Morais, J. P. S., Brígida, A. I. S., Muniz, C. R., et al. (2015). Development of chlorine-free pulping method to extract cellulose nanocrystals from pressed oil palm mesocarp fibers. *Journal of Biobased Materials and Bioenergy, 9*(3), 372–379.

Sugiyama, J., Persson, J., & Chanzy, H. (1991). Combined infrared and electron diffraction study of the polymorphism of native celluloses. *Macromolecules, 24*(9), 2461–2466.

Sun, J. X., Sun, X. F., Zhao, H., & Sun, R. C. (2004). Isolation and characterization of cellulose from sugarcane bagasse. *Polymer Degradation and Stability, 84*(2), 331–339.

Tang, Y., Yang, H., & Vignolini, S. (2022). Recent progress in production methods for cellulose nanocrystals: leading to more sustainable processes. *Advanced Sustainable Systems*, Article 2100100.

Trache, D., Hussin, M. H., Haafiz, M. K. M., & Thakur, V. K. (2017). Recent progress in cellulose nanocrystals: Sources and production. *Nanoscale, 9*(5), 1763–1786.

Wang, Y., Xie, R., Zheng, S., Zhou, N., Lu, J., Ahmad, I., et al. (2021). Nonuniformly modifying high-aspect-ratio rigid cellulose nanocrystals to enhance percolation advantage in weakly compatible biomass polymer systems. *Cellulose (London, England)*, 1–15.

Wei, X.-. L., Fahlman, M., & Epstein, A. J. (1999). XPS study of highly sulfonated polyaniline. *Macromolecules, 32*(9), 3114–3117.

Wu, S., Ning, D., Xu, D., Cheng, Y., Mondal, A. K., Zou, Q., et al. (2022). Preparation and characterization of super hydrophobic aerogels derived from tunicate cellulose nanocrystals. *Carbohydrate Research, 511*, Article 108488.

Wüstenberg, T. (2014). *Cellulose and cellulose derivatives in the food industry: Fundamentals and applications*. John Wiley & Sons.

Yang, S.-. Y., Lin, W.-. N., Huang, Y.-. L., Tien, H.-. W., Wang, J.-. Y., Ma, C.-C. M., et al. (2011). Synergetic effects of graphene platelets and carbon nanotubes on the mechanical and thermal properties of epoxy composites. *Carbon, 49*(3), 793–803.

Yunos, N. S. H. M., Baharuddin, A. S., Yunos, K. F. M., Naim, M. N., & Nishida, H. (2012). Physicochemical property changes of oil palm mesocarp fibers treated with high-pressure steam. *Bioresources, 7*(4), 5983–5994.

Zhang, L., Lu, Z., Velarde, L., Fu, L., Pu, Y., Ding, S.-. Y., et al. (2015). Vibrational spectral signatures of crystalline cellulose using high resolution broadband sum frequency generation vibrational spectroscopy (HR-BB-SFG-VS). *Cellulose (London, England), 22*(3), 1469–1484.

Zhao, Y., & Li, J. (2014). Excellent chemical and material cellulose from tunicates: Diversity in cellulose production yield and chemical and morphological structures from different tunicate species. *Cellulose (London, England), 21*(5), 3427–3441.

Zhao, Y., Moser, C., Lindström, M. E., Henriksson, G., & Li, J. (2017). Cellulose nanofibers from softwood, hardwood, and tunicate: Preparation–structure–film performance interrelation. *Acs Applied Materials & Interfaces, 9*(15), 13508–13519.

Zhou, L., He, H., Li, M., Huang, S., Mei, C., & Wu, Q. (2018). Enhancing mechanical properties of poly (lactic acid) through its in-situ crosslinking with maleic anhydride-modified cellulose nanocrystals from cottonseed hulls. *Industrial Crops and Products, 112*, 449–459.